OPTICA

Acoustic-feedback wavefront-adapted photoacoustic microscopy

Yuecheng Shen,[1,†] **Jun Ma,**[2,†] **Chengtian Hou,**[2,†] **Jiayu Zhao,**[3] **Yan Liu,**[4,7]
Hsun-Chia Hsu,[5] **Terence T. W. Wong,**[6] **Bai-Ou Guan,**[2] **Shian Zhang,**[1,8]
and Lihong V. Wang[5,9]

[1]*State Key Laboratory of Precision Spectroscopy, School of Physics and Electronic Science, East China Normal University, Shanghai 200241, China*
[2]*Guangdong Provincial Key Laboratory of Optical Fiber Sensing and Communications, College of Physics & Optoelectronic Engineering, Jinan University, Guangzhou 510632, China*
[3]*School of Electronics and Information Technology, Sun Yat-Sen University, Guangzhou 510275, China*
[4]*School of Optometry, Indiana University, Bloomington, Indiana 47405, USA*
[5]*Caltech Optical Imaging Laboratory, Andrew and Peggy Cherng Department of Medical Engineering, Department of Electrical Engineering, California Institute of Technology, 1200 East California Boulevard, Pasadena, California 91125, USA*
[6]*Translational and Advanced Bioimaging Laboratory, Department of Chemical and Biological Engineering, Hong Kong University of Science and Technology, Hong Kong SAR, China*
[7]*yl144@iu.edu*
[8]*sazhang@phy.ecnu.edu.cn*
[9]*lvw@caltech.edu*
[†]*These authors contributed equally to this work.*

Optical microscopy is indispensable to biomedical research and clinical investigations. As all molecules absorb light, optical-resolution photoacoustic microscopy (PAM) is an important tool to image molecules at high resolution without labeling. However, due to tissue-induced optical aberration, the imaging quality degrades with increasing imaging depth. To mitigate this effect, we develop an imaging method, called acoustic-feedback wavefront-adapted PAM (AWA-PAM), to dynamically compensate for tissue-induced aberration at depths. In contrast to most existing adaptive optics assisted optical microscopy, AWA-PAM employs acoustic signals rather than optical signals to indirectly determine the optimized wavefront. To demonstrate this technique, we imaged zebrafish embryos and mouse ears *in vivo*. Experimental results show that compensating for tissue-induced aberration in live tissue effectively improves both signal strength and lateral resolution. With this capability, AWA-PAM reveals fine structures, such as spinal cords and microvessels, that were otherwise unidentifiable using conventional PAM. We anticipate that AWA-PAM will benefit the *in vivo* imaging community and become an important tool for label-free optical imaging in the quasi-ballistic regime. © 2024 Optica Publishing Group under the terms of the Optica Open Access Publishing Agreement

1. INTRODUCTION

Optical microscopy is crucial to many science and engineering fields. As all molecules absorb light, photoacoustic (PA) microscopy (PAM) is an important technique that employs non-ionizing photons and low-scattering ultrasound to image molecules. By offering universal optical absorption contrast, deep penetration, and label-free capability, PAM is suitable for a wide range of biomedical applications, such as functional imaging of blood oxygenation, tracking of circuiting tumor cells, lipid imaging, and label-free histology [1–6]. PAM involves both optical excitation and acoustic detection, thereby providing a great diversity of embodiments. When biological tissue is probed with a pulsed and focused light beam, acoustic waves are generated due to absorption-induced heat generation, thus revealing cellular or even sub-cellular structures with high spatial resolution determined by the optical diffraction limit. This modality, termed optical-resolution photoacoustic microscopy (OR-PAM), was first developed in 2008 to image microvasculatures in mice *in vivo* [7]. However, biological tissue is inherently heterogeneous, which distorts the optical wavefront and causes optical aberration as light propagates through. Since the performance of OR-PAM strongly relies on the quality of the excitation focus, it inevitably suffers from degradations in both PA amplitude and spatial resolution while imaging at depths.

In general, optical aberration deteriorates the imaging performance of all optical microscopy. To alleviate this issue, adaptive optics (AO), which was initially developed in astronomy to compensate for atmosphere-induced aberration, has been introduced into optical microscopy. By actively modulating the incident

wavefront to compensate for both system-generated and tissue-induced aberration, AO has become an effective tool for improving image quality. To date, AO has been widely adopted in widefield microscopy [8–13] and point-scanning microscopy [14–23] such as confocal and multiphoton microscopy. There are a variety of implementations of AO schemes to determine the distorted wavefront, including measuring the optical wavefront directly by using a Shack-Hartmann (SH) sensor [9,11,15,16,19,24–26] and reconstructing the optical wavefront indirectly through pupil segmentation approaches [17,18,27–29], which have been well discussed and summarized in recent reviews [30–33]. In addition, optical aberration can also be determined by iteratively adjusting the wavefront until a certain image metric is optimized [34–42]. In all these existing implementations, optical measurements concerning either back-reflected excitation light or emitted fluorescent light are required to determine the optical aberration.

OR-PAM relies on optical focusing to achieve high lateral resolution and acoustic time-of-arrival to achieve high axial resolution; it produces a one-dimensional (1D) depth-resolved image (an A-line) per laser pulse. Therefore, the quality of the excitation optical focus is crucially important to the performance of OR-PAM. The first attempt to introduce AO into OR-PAM was in 2010, which aims to correct system-generated aberration [43]. By employing an SH sensor to directly measure the backscattered light from a white paper and a deformable mirror (DM) to compensate for the system-generated aberration, significant improvements in both signal strength and lateral resolution were demonstrated [43]. In 2022, AO was employed to compensate for the spherical aberration caused by the mismatch of refractive indices between water and a target sample, by using a three-layer liquid crystal device optimized for correcting this specific aberration mode [44]. Despite these efforts, however, using AO to correct tissue-induced aberration in OR-PAM has not been demonstrated. This situation may be due to the lack of appropriate guide stars in PAM. On one

hand, back-scattered excitation light does not function well, as the back-reflected light may come from different regions from the focal volume. On the other hand, the widely used fluorescent signals do not naturally exist in PAM. To fill this void, we develop acoustic-feedback wavefront-adapted PAM (AWA-PAM), which employs acoustic feedback to correct for tissue-induced optical aberration in OR-PAM. In contrast to other AO assisted three-dimensional (3D) optical microscopy techniques that generally abandon the correction for defocus to avoid axial shifting [45], AWA-PAM delightfully takes the correction of defocus into consideration. This choice is because the depth information of PAM is uniquely determined by the time of arrival of the acoustic waves. In this condition, optimizing the depth of the focal plane for each A-line can considerably benefit the imaging of small features at different depths across the field of view. To demonstrate the feasibility of AWA-PAM, we built a microscope system by integrating a liquid crystal based spatial light modulator and an OR-PAM system. The tissue-induced aberration was dynamically compensated point-by-point by optimizing the phase map displayed on the SLM with a greedy algorithm. We will show in the next section that AWA-PAM effectively corrects for tissue-induced aberration when imaging *in vivo* zebrafish embryos and mouse ears and significantly improves the image quality, revealing microstructures that are indiscernible with conventional PAM.

2. RESULTS

A. Principle of AWA-PAM

We start by describing the operational principle of AWA-APM, which is schematically shown in Fig. 1. In conventional PAM, as shown in Fig. 1(a), pulsed light is focused into the biological tissue to locally induce ultrasonic waves, which are subsequently detected by a focused ultrasonic transducer through confocal geometry. The peak-to-valley value of the measured ultrasonic wave, defined as
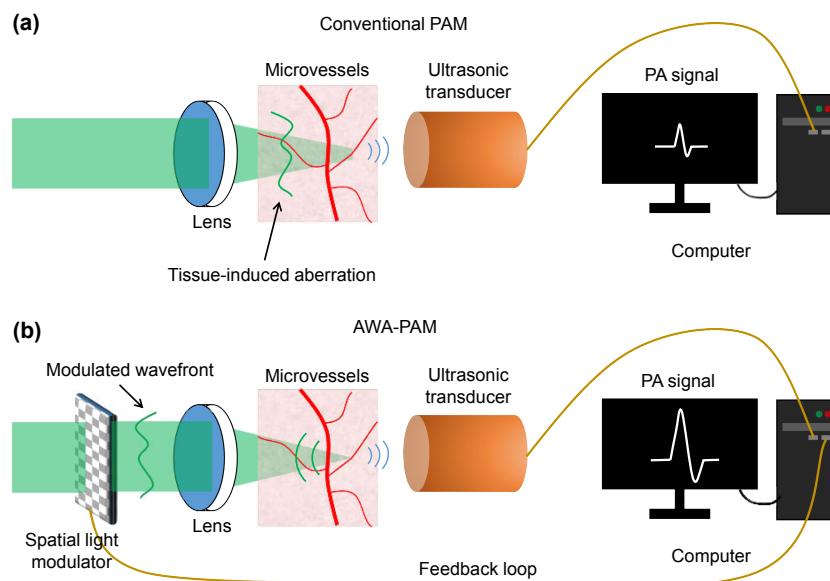

Fig. 1. Schematics of the operational principle of AWA-PAM. (a) In conventional PAM, pulsed light is focused into the biological tissue to locally induce ultrasonic waves, which are measured by a focused ultrasonic transducer. The heterogeneity of the biological tissue distorts the wavefront of the focused light, decreasing the signal strength and resolution. (b) In AWA-PAM, a spatial light modulator modulates the wavefront of the pulsed excitation light to compensate for tissue-induced aberration. The phase map displayed by the SLM is the inverse phase of the distorted wavefront, thereby nullifying the distortion and creating a sharp focus at depths. To obtain the desired phase map, a feedback loop between the SLM, the computer, and the ultrasonic transducer is established to optimize the PA amplitude.

the PA amplitude, is generally used to reflect the local absorption of the tissue within the optical focus. In this condition, the full width at half maximum (FWHM) size of the optical focus determines the lateral resolution. In practice, however, optical aberration aggregates as the excitation light propagates due to the heterogeneity of biological tissue, which broadens the focus and deteriorates the resolution. Moreover, as light is not tightly focused and energy is not highly concentrated, the measured PA amplitude also decreases for small features. As a result, tissue-induced aberration deteriorates both lateral resolution and signal strength.

Inspired by the effectiveness of adaptive optics in fighting against tissue-induced optical aberration in optical microscopy, we developed AWA-PAM to effectively mitigate this issue, as shown in Fig. 1(b). The key enabling point is to modulate the excitation light by using an SLM before it enters the tissue. One would expect that tissue-induced aberration can be compensated by modulating the incident wavefront, resulting in a sharp focus at depths. Due to the special detecting scheme with ultrasound, AWA-PAM adopts an indirect wavefront sensing approach by employing acoustic feedback to estimate the desired phase map through a greedy optimization algorithm. To begin with, the SLM displays a planar phase map such that AWA-PAM effectively functions as conventional PAM. Then, a series of ordered Zernike polynomials are loaded to the SLM in order. These Zernike polynomials are orthogonal to each other over circular pupils [46], and each one effectively represents one type of optical aberration. A feedback loop is established among the SLM, the ultrasonic transducer, and the computer. The corresponding coefficients for each order of the Zernike polynomials are traversed and determined in an ergodic manner [47,48]. This feedback loop guarantees continuous enhancement in PA amplitudes after correcting aberrations for each order, leading to the formation of a high-quality focus eventually. The AWA-PAM is relatively simple and does not require direct optical wavefront sensing to determine tissue-induced aberration, which is particularly suitable for PAM with ultrasonic detection. This process is essentially similar to that of feedback-based wavefront shaping with acoustic feedback [49–52]. However, the scattering process inside biological tissue is almost random, which requires a large number of modes to be tested to generate a focus with acceptable quality. Thus, this inefficient method makes it almost impossible to implement for *in vivo* studies. In comparison, optical aberrations are known to be well-represented by the Zernike polynomials. In this condition, the feedback process is quite efficient, as one needs to consider only a few low-order Zernike polynomials to account for optical aberration. Therefore, point-by-point compensation for spatially inhomogeneous optical aberration can be realized even for live tissue. Furthermore, some of the previous works allow only focusing light to indefinite locations and are not suitable for 3D imaging, unlike AWA-PAM.

B. Compensating for System Aberration

We first compensate for the system aberration by imaging a carbon fiber. The experimental setup of AWA-PAM is schematically shown in Fig. 2(a) with a detailed description in Appendix A. To guarantee sufficient accuracy under static conditions, the step size for traversing the coefficients for a given Zernike mode was set to 0.2π rads, and the range was from -10π to $+10\pi$ rads. Phase wrapping was performed. Using PA amplitudes as feedback, Fig. 2(b) shows the signal enhancement contributed from each order. Among them, the 1st order (i.e., piston) has no effect, while the 2nd and 3rd orders that correspond to tip and tilt are the two largest contributors. These two corrections mainly account for the misalignment of the SLM. Besides, the correction for the 4th order that corresponds to defocus helps, possibly due to correction for the curvature of the SLM, the use of a lens pair and depth-induced aberration. Corrections for the Zernike polynomials from the 5th order to the 8th order also provide certain contributions. In contrast, the Zernike polynomials after the 10th order have negligible effects, indicating that high-order aberration does not exist in the current system. Overall, compensating for system aberration effectively enhances PA amplitudes by about three times. The image of the focus shown in Fig. 2(c) confirms that, in free space, the lateral resolution can be brought back to the theoretically predicted $\sim 3\,\mu m$ after correcting for the system aberration. Since system-generated aberration is static, a fixed phase map corresponding to correcting the system aberration is always used as the initial phase map before subsequent wavefront optimization to correct for sample-induced aberration.

C. Imaging Spinal Cords of Zebrafish Embryos *In Vivo*

The feasibility of AWA-PAM to compensate for tissue-induced aberration was demonstrated through imaging spinal cords of zebrafish embryos *in vivo*. The zebrafish used for imaging is two days after fertilization. After anesthetizing the zebrafish, we first performed whole-body imaging through conventional PAM, which is shown in Fig. 3(a). Then, we proceeded to execute AWA-PAM to demonstrate its superiority in revealing structures that were hindered by optical aberrations. Given that imaging the whole fish is time-consuming, wavefront correction was performed on a smaller region that mainly contains the spinal cord, which is denoted by the white dashed square in Fig. 3(a). To avoid causing artifacts due to beam drifting, we restrict the orders of the Zernike polynomials from 4 to 10 (i.e., excluding tip, tilt, and piston) during *in vivo* experiments. The step size of the coefficient for traversing each Zernike order was set to π rads, and the optimization range was from -4π to $+4\pi$ rads. The isoplanatic patch size was measured to be $15 \times 15\,\mu m^2$ (with the quantification procedures described in Supplement 1, Note 1) and we used the same corrective wavefront for the measurements taken within the isoplanatic patch. Higher Zernike orders, smaller step sizes, finer isoplanatic patches, and larger optimization ranges can be targeted, which is at the cost of increased imaging time and will be discussed later. Figures 3(b) and 3(c) show the obtained 3D image and its corresponding 2D maximum amplitude projection (MAP) image of the spinal cords of the zebrafish embryo by employing AWA, respectively. As a comparison, the obtained 3D image and 2D MAP image for the same region without using AWA correction are shown in Figs. 3(d) and 3(e), respectively. It is clear that AWA-PAM provides richer structural information than that obtained without AWA correction. Notably, AWA correction includes the adjustment of the 4th order of the Zernike polynomials that represents defocusing, allowing spinal cords at different depths to be identified. Such an implementation presents a key difference between AWA-PAM and other AO-assisted 3D optical microscopy. For example, the spinal cord enclosed within the white dashed box in Fig. 3(c) could hardly be seen without AWA correction [Fig. 3(e)] but becomes visible with the assistance of AWA correction. The depth information for the 2D MAP image acquired with AWA correction [Fig. 3(c)] was extracted based on the time-of-flight information of the ultrasonic wave and provided in Fig. 3(f).
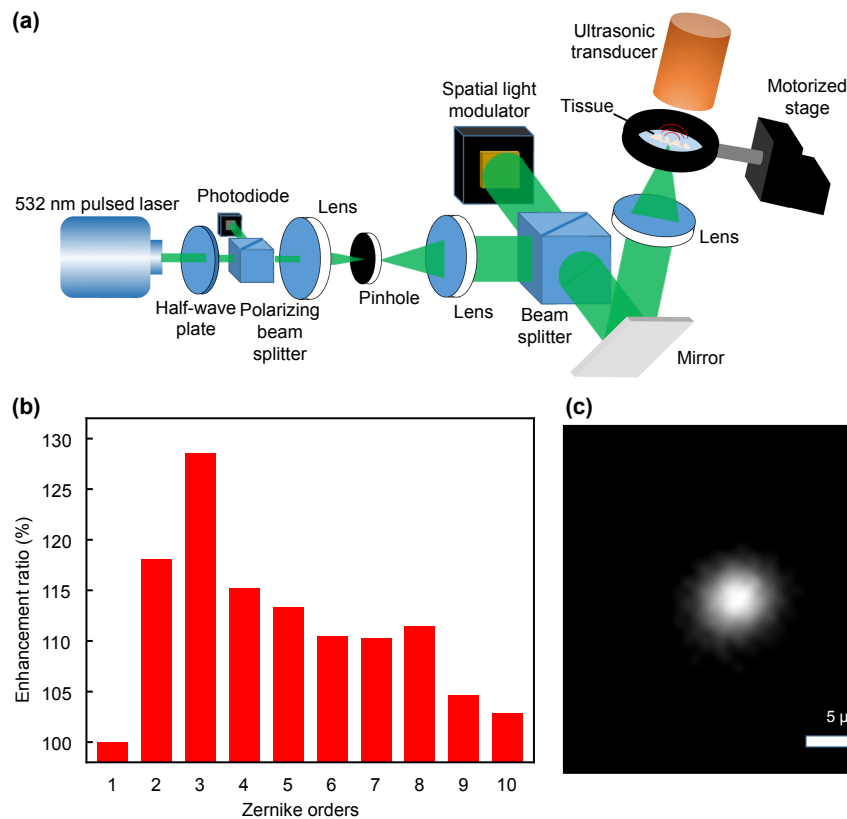
Fig. 2. Compensating for inherent system aberration. (a) Schematic illustration of the AWA-PAM system. The light being focused into the tissue is modulated by a spatial light modulator, which dynamically compensates for spatially inhomogeneous tissue-induced aberration. (b) Signal enhancement contributed by each order of Zernike modes. (c) An image of the focus after compensation for system aberration, captured through an optical microscope.

This image shows that different spinal cords are indeed located at different depths. Detailed information on the optimization performance and phase maps at different locations can be found in Supplement 1, Note 2.

D. Imaging Microvascular Structures of Mouse Ear *In Vivo*

The effectiveness of AWA-PAM was also demonstrated by imaging microvascular structures of mouse ears *in vivo*. The mouse was anesthetized by isoflurane during the entire experiment, and the ear to be imaged was in a natural state, i.e., without being pressed or flattened, which can otherwise restrain blood flow. The same setting used for imaging zebrafish embryos was used here. Figures 4(a) and 4(b) show the 3D microvascular images of the mouse ear from two different views obtained with AWA correction, and its corresponding 2D MAP image is also shown in Fig. 4(c). In comparison, 3D images and corresponding 2D MAP image obtained without AWA correction are illustrated in Figs. 4(d)–4(f). Although big vessels can be identified in both images, the AWA correction effectively helps to identify microvascular structures at depths. For example, by scrutinizing the regions highlighted by the white dashed boxes in Fig. 4(c), one could hardly see similar features in the same regions in the image obtained without AWA correction [Fig. 4(f)]. Moreover, by comparing the MAP images belonging to different categories, we note that signal strengths obtained with AWA correction are generally stronger than those obtained without AWA correction. Furthermore, Figs. 4(g) and 4(h) plot the profiles along the two white dashed lines labeled in Figs. 4(c) and 4(f). A

direct comparison shows that richer structural information can be observed with AWA correction (the red solid curve). In contrast, the 1D profiles obtained without AWA correction, denoted by the dashed blue curves, are almost informationless. As before, for the 2D MAP image with AWA correction activated, the depth information based on the time-of-flight information of the ultrasonic wave is provided in Fig. 4(i). As we can see from the figure, microvascular structures that are hardly seen in Fig. 4(f) are at a depth that is distinctively different from the focal plane (13.1 mm). These observations demonstrate the superior performance of AWA-PAM over conventional PAM in revealing microstructures that are wiped out by optical aberrations. Detailed information on the optimization performance and phase maps at different locations can be found in Supplement 1, Note 3.

3. DISCUSSION

In principle, AWA-PAM relies on the assumption that the tightest focus produces the strongest PA amplitude. Unlike two-photon fluorescent microscopy, which employs nonlinearity, PA is generally considered a linear process. Nonetheless, when imaging capillaries in practice, Supplement 1, Note 4 suggests that the lateral resolution degrades to tens of microns at the depths of a few hundred microns. Since the lateral resolution without AWA correction is larger than the diameters of many capillaries, AWA-PAM can increase the PA amplitude and achieve a tighter focus, thus revealing more microscopic features. Moreover, even for very big vessels shown in Fig. 4, we found a roughly 20%–30% signal enhancement by using AWA correction (detailed in
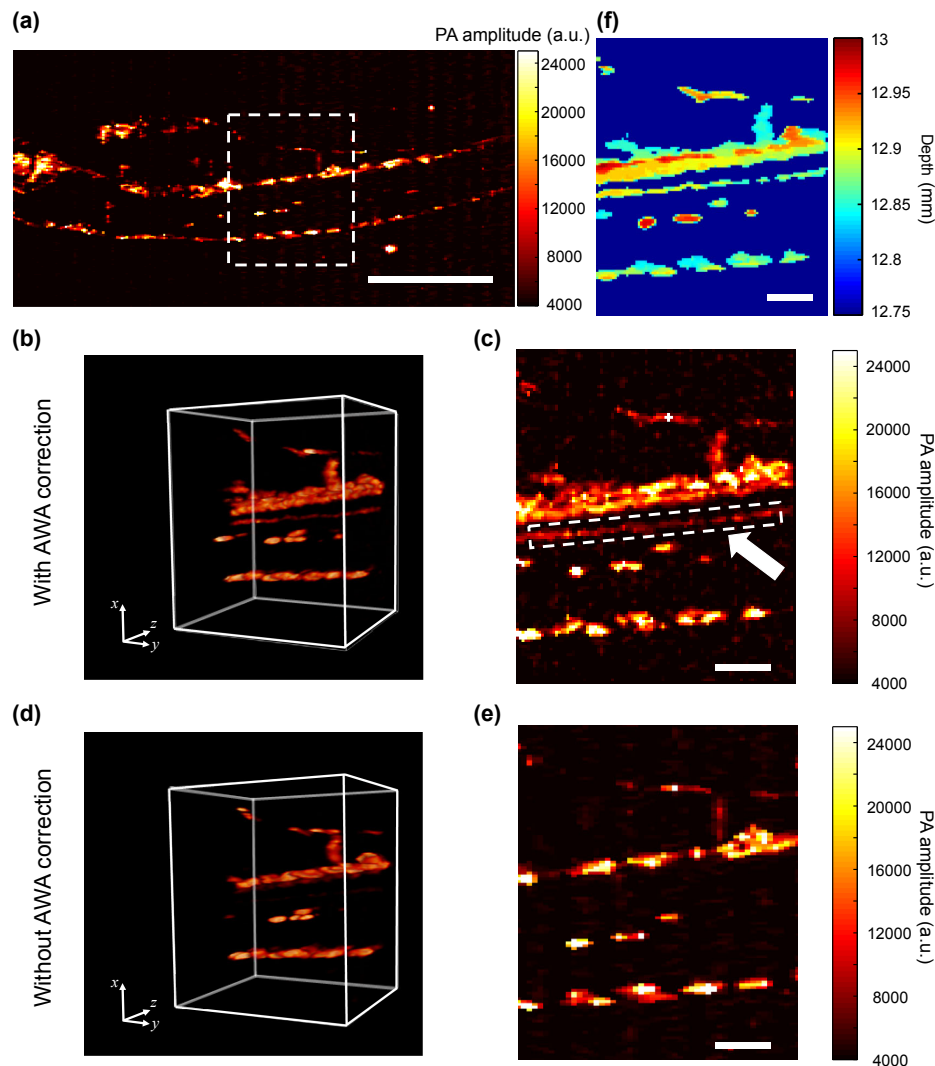
Fig. 3. *In vivo* imaging of zebrafish embryos. (a) Whole-body image of the zebrafish embryo, captured through conventional PAM. The white dashed square denotes the area of interest with spinal cords. Scale bar: 500 µm. (b) 3D image and (c) its 2D MAP image of the area highlighted in (a) obtained with AWA correction. Image sizes: $0.60 \times 0.50 \times 0.45$ mm^3 (x, y, z). Scale bar, 100 µm. (d) 3D image and (e) its 2D MAP image of the area highlighted in (a) obtained without AWA correction. Image sizes: $0.60 \times 0.50 \times 0.45$ mm^3 (x, y, z). Scale bar, 100 µm. (f) Depth information of the microstructures in the 2D MAP image in (c). Scale bar, 100 µm.

Supplement 1, Note 5). This observation is likely because a tighter focus produces more high-frequency components, which leads to larger signal strengths in OR-PAM where high-frequency ultrasonic transducers are generally employed [53–55]. It is also worth mentioning that the optical focusing depth was adjusted in AWA-PAM, which is very different from the procedures in conventional AO-assisted 3D microscopy. Such an operation takes advantage of the acoustic detection in PAM and the sparsity of the sample along the depth direction, which is generally true for many biological tissues including vasculatures in mouse ears. In this context, the imaging depth range of AWA-PAM can reach acoustic depth of focus, which is much larger than the optical depth of focus. In short, since PAM detects ultrasound instead of light, using acoustic signals rather than optical signals as a feedback metric is a natural choice. Moreover, the generation of acoustic signals is a rather complicated process that involves light, heat, and sound; the validity of AWA-PAM also relies on the fact that the distribution of the acoustic property of the sample is much more uniform than that of the optical property.

The imaging speed of AWA-PAM can be further improved in future studies. In the current practice, seven measurements were made to determine the optimum coefficients for each Zernike order. With certain prior knowledge of the extent of aberration and a sufficiently high signal-to-noise ratio, $3N$ or even $2N + 1$ measurement could be enough to determine the coefficients of N orders [41,45]. Such a decrease in the number of measurements, albeit at the cost of determination accuracy, can effectively improve the imaging speed. Second, for the current imaging system, the bottleneck of the system speed is the low refreshing rate of the SLM (60 Hz). Consequently, optimizing the coefficients of the Zernike polynomials (locating the inflection point) leads to an averaged A-line scanning rate of 1 Hz. Thus, taking the imaging process of mouse ears as an example, acquiring a two-dimensional image of 1 mm^2 takes about 37 min. Although this duration is much longer than that consumed by conventional PAM, AWA-PAM can be further sped up by using micro-electro-mechanical-system-based SLMs that operate up to hundreds of kHz [56–59], allowing two-dimensional images of 1 mm^2 to be formed within ten seconds.
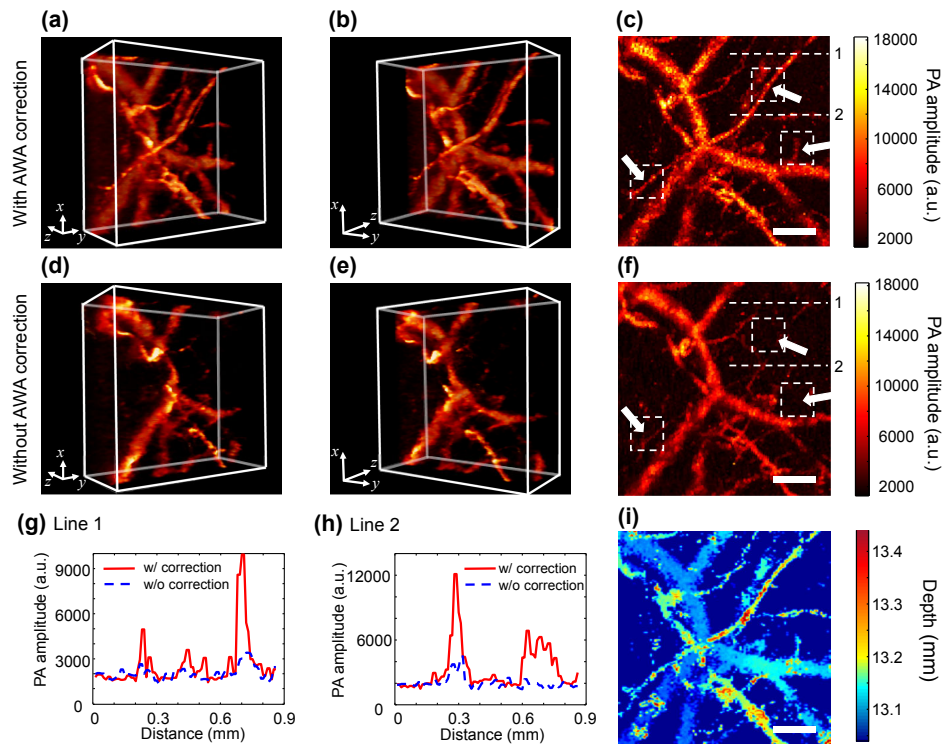
Fig. 4. *In vivo* imaging of mouse ears in the natural state. (a), (b) Two different views of the 3D microvascular images obtained with AWA correction. Image sizes: $1.00 \times 1.00 \times 0.40$ mm^3 (x, y, z). (c) Corresponding 2D MAP image obtained with AWA correction. Scale bar, 200 μm. (d), (e) Two different views of the 3D microvascular images obtained without AWA correction. Image sizes: $1.00 \times 1.00 \times 0.40$ mm^3 (x, y, z). (f) Corresponding 2D MAP image obtained without AWA correction. Scale bar, 200 μm. (g), (h) Line profiles of the dashed lines in (c) and (f) for the microvascular structures obtained with (red) and without (blue) AWA correction. Scale bars, 200 μm. (i) Depth information of the microvascular structures in the 2D MAP image in (c). Scale bar, 200 μm.

Imaging speed can be further improved by choosing an adaptive scanning strategy. For example, by tracking the vessels' profile [60], one can perform fine compensations for optical aberration only in those regions that are of particular interest. Given that more than 60% of the area is informationless, the imaging time could be further reduced with this strategy. To demonstrate the principle, the current system was built in transmission mode. A reflection-mode system will be built in the future to adapt AWA-PAM for various applications [61–63].

In this study, AWA-PAM was demonstrated using an imaging system with a numerical aperture (NA) of 0.1 (which is the most widely used value), leading to a 3 μm resolution under the aberration-free condition. The principle of AWA-PAM works for different NAs, and the adaptive correction should be more critical for larger NAs. While it is difficult to characterize resolution enhancement for *in vivo* studies, this enhancement may be quantified through the employment of tissue-mimicking phantoms with controlled thickness. As detailed in Supplement 1, Note 4, experimental results show that AWA-PAM effectively improves the lateral resolution at all depths tested. In particular, it achieves nearly two-fold improvement in lateral resolution in comparison to conventional PAM at a depth range of 150–200 μm. Nonetheless, since scattering phantoms are mesoscopic homogeneous and do not induce strong optical aberration, we consider the obtained values may be conservative compared to the ones achieved during *in vivo* experiments. Moreover, as illustrated in Supplement 1, Note 4, AWA-PAM exclusively operates within the quasi-ballistic regime, unable to address optical scattering. Beyond imaging

depths of 1 mm in soft tissue, AWA-PAM diminishes its efficacy, and the resolution eventually becomes acoustically determined.

In conclusion, we have developed AWA-PAM to compensate for tissue-induced aberration dynamically. Endogenous optical absorptive objects are employed as internal guide stars to provide acoustic feedback in order to characterize spatially inhomogeneous optical aberration. The feasibility of AWA-PAM was experimentally demonstrated on both zebrafish embryos and mouse ears *in vivo*. Considerable improvements in both lateral resolution and signal strength were observed, showing that AO effectively helps PAM to generate a more intensified and localized focus at depths. We envision that the demonstrated approach will serve as a useful tool for label-free optical imaging in the quasi-ballistic regime.

APPENDIX A: METHODS

1. Experimental Setup

A pulsed laser (Changchun New Industries, MPL-H-532-30 μJ) operating at 532 nm was used as a light source. A halfwave plate (Thorlabs, WPH05ME-532) and a polarizing beam splitter (Thorlabs, PBS532) controlled the power being dumped into the system and set the output light to be horizontally polarized. The laser has pulse-to-pulse intensity fluctuations up to 10%, which can potentially contaminate the feedback signal. To address this issue, a photodiode (Thorlabs, SM1PA1A) was employed to monitor the intensity of the reflected light from the polarizing beam splitter, and the measured value was used for normalization. Then, the laser beam was expanded through a pair of lenses

(Thorlabs, LB1761, focal length: 25.4 mm; Thorlabs, LB1437, focal length: 150 mm) and spatially filtered by a pinhole placed at the focal plane. A liquid-crystal SLM (Holoeye, Pluto-VIS-016, 1920×1080 pixels, 8 µm pixel size) working in reflection mode was employed for wavefront modulation. After reflection from the SLM, light was then focused into the tissue through a lens (Thorlabs, LB1901). The illuminating system has an NA of about 0.1, leading to an optical focus with a theoretical FWHM spot size of about $0.51\lambda/\text{NA} = 2.7$ µm. After light absorption by tissue, ultrasonic wave was emitted and collected by a focused 25 MHz ultrasonic transducer (Olympus, V324-N-SU, $\text{NA}_a = 0.23$). The received PA amplitudes were amplified, filtered, and then digitized by a data acquisition system (not shown in the figure). Three-dimensional images were formed by raster-scanning the sample, which was realized through a motorized stage (PI, L-509.20SD00). Depth information was obtained through the time-of-arrival of the acoustic wave; hence, no z-scanning is required in PAM. Theoretically, the FWHM sizes of the acoustic focus along the lateral and axial directions are $0.71\lambda_a/\text{NA}_a = 185$ µm and $2.4\lambda_a/\text{NA}_a^2 = 2.7$ mm, where $\lambda_a = 60$ µm is the acoustic wavelength and $\text{NA}_a = 0.23$ is the acoustic NA. Two-dimensional images were generated by maximum intensity projection of the 3D volume. The software was developed in-house for controlling all the devices.

2. *In Vivo* Animal Study

The animal study was carried out in conformity with laboratory animal protocols approved by the Animal Studies Committee of Jinan University. An 8-week-old BALB/c female mouse was used for the *in vivo* experiment. Throughout the experiment, the mouse was anesthetized by 1.5% vaporized isoflurane during the entire experiment. The 1-phenyl 2-thiourea treated zebrafish embryo (72 h post fertilization) was anesthetized with tricaine and then embedded into a small amount of zebrafish body positioning solution (0.1 mL). The posture of the embryo was adjusted and placed in water for PAM imaging.

Data availability. All data needed to evaluate the conclusions in the paper are present in the main text and Supplement 1. Additional data are available from authors upon request.

Supplemental document. See Supplement 1 for supporting content.

REFERENCES

1. S. Sethuraman, J. H. Amirian, S. H. Litovsky, *et al.*, "Spectroscopic intravascular photoacoustic imaging to differentiate atherosclerotic plaques," Opt. Express **16**, 3362–3367 (2008).
2. Y. He, L. Wang, J. Shi, *et al.*, "In vivo label-free photoacoustic flow cytography and on-the-spot laser killing of single circulating melanoma cells," Sci. Rep. **6**, 39616 (2016).
3. H.-C. Hsu, L. Wang, and L. V. Wang, "In vivo photoacoustic microscopy of human cuticle microvasculature with single-cell resolution," J. Biomed. Opt. **21**, 056004 (2016).
4. J. Yao and L. V. Wang, "Photoacoustic microscopy," Laser Photon. Rev. **7**, 758–778 (2013).
5. T. T. W. Wong, R. Zhang, P. Hai, *et al.*, "Fast label-free multilayered histology-like imaging of human breast cancer by photoacoustic microscopy," Sci. Adv. **3**, e1602168 (2017).
6. R. Cao, J. Li, Y. Kharel, *et al.*, "Photoacoustic microscopy reveals the hemodynamic basis of sphingosine 1-phosphate-induced neuroprotection against ischemic stroke," Theranostics **8**, 6111–6120 (2018).
7. K. Maslov, H. F. Zhang, S. Hu, *et al.*, "Optical-resolution photoacoustic microscopy for in vivo imaging of single capillaries," Opt. Lett. **33**, 929–931 (2008).
8. D. Débarre, E. J. Botcherby, M. J. Booth, *et al.*, "Adaptive optics for structured illumination microscopy," Opt. Express **16**, 9290–9305 (2008).
9. O. Azucena, J. Crest, J. Cao, *et al.*, "Wavefront aberration measurements and corrections through thick tissue using fluorescent microsphere reference beacons," Opt. Express **18**, 17521–17532 (2010).
10. C. Bourgenot, C. D. Saunter, J. M. Taylor, *et al.*, "3D adaptive optics in a light sheet microscope," Opt. Express **20**, 13252–13261 (2012).
11. R. Jorand, G. Le Corre, J. Andilla, *et al.*, "Deep and clear optical imaging of thick inhomogeneous samples," PLoS ONE **7**, e35795 (2012).
12. Z. Li, Q. Zhang, S.-W. Chou, *et al.*, "Fast widefield imaging of neuronal structure and function with optical sectioning in vivo," Sci. Adv. **6**, eaaz3870 (2020).
13. S. A. Hussain, T. Kubo, N. Hall, *et al.*, "Wavefront-sensorless adaptive optics with a laser-free spinning disk confocal microscope," J. Microsc. **288**, 106–116 (2022).
14. M. J. Booth, M. A. A. Neil, R. Juškaitis, *et al.*, "Adaptive aberration correction in a confocal microscope," Proc. Natl. Acad. Sci. USA **99**, 5788–5792 (2002).
15. J.-W. Cha, J. Ballesta, and P. T. So, "Shack-Hartmann wavefront-sensor-based adaptive optics system for multiphoton microscopy," J. Biomed. Opt. **15**, 046022 (2010).
16. X. Tao, B. Fernandez, O. Azucena, *et al.*, "Adaptive optics confocal microscopy using direct wavefront sensing," Opt. Lett. **36**, 1062–1064 (2011).
17. C. Wang and N. Ji, "Pupil-segmentation-based adaptive optical correction of a high-numerical-aperture gradient refractive index lens for two-photon fluorescence endoscopy," Opt. Lett. **37**, 2001–2003 (2012).
18. C. Wang and N. Ji, "Characterization and improvement of three-dimensional imaging performance of GRIN-lens-based two-photon fluorescence endomicroscopes with adaptive optics," Opt. Express **21**, 27142–27154 (2013).
19. S. A. Rahman and M. J. Booth, "Direct wavefront sensing in adaptive optical microscopy using backscattered light," Appl. Opt. **52**, 5523–5532 (2013).
20. S. Yoon, H. Lee, J. H. Hong, *et al.*, "Laser scanning reflection-matrix microscopy for aberration-free imaging through intact mouse skull," Nat. Commun. **11**, 5721 (2020).
21. C. Rodríguez, A. Chen, J. A. Rivera, *et al.*, "An adaptive optics module for deep tissue multiphoton imaging in vivo," Nat. Methods **18**, 1259–1264 (2021).
22. L. Streich, J. C. Boffi, L. Wang, *et al.*, "High-resolution structural and functional deep brain imaging using adaptive optics three-photon microscopy," Nat. Methods **18**, 1253–1258 (2021).
23. X. Hao, E. S. Allgeyer, D.-R. Lee, *et al.*, "Three-dimensional adaptive optical nanoscopy for thick specimen imaging at sub-50-nm resolution," Nat. Methods **18**, 688–693 (2021).
24. R. Aviles-Espinosa, J. Andilla, R. Porcar-Guezenec, *et al.*, "Measurement and correction of in vivo sample aberrations employing a nonlinear guide-star in two-photon excited fluorescence microscopy," Biomed. Opt. Express **2**, 3135–3149 (2011).
25. K. Wang, D. E. Milkie, A. Saxena, *et al.*, "Rapid adaptive optical recovery of optimal resolution over large volumes," Nat. Methods **11**, 625–628 (2014).
26. K. Wang, W. Sun, C. T. Richie, *et al.*, "Direct wavefront sensing for high-resolution in vivo imaging in scattering tissue," Nat. Commun. **6**, 7276 (2015).
27. N. Ji, D. E. Milkie, and E. Betzig, "Adaptive optics via pupil segmentation for high-resolution imaging in biological tissues," Nat. Methods **7**, 141–147 (2009).
28. J. Scrimgeour and J. E. Curtis, "Aberration correction in wide-field fluorescence microscopy by segmented-pupil image interferometry," Opt. Express **20**, 14534–14541 (2012).

29. R. Liu, D. E. Milkie, A. Kerlin, *et al.*, "Direct phase measurement in zonal wavefront reconstruction using multidither coherent optical adaptive technique," Opt. Express **22**, 1619–1628 (2014).

30. M. J. Booth, "Adaptive optical microscopy: the ongoing quest for a perfect image," Light Sci. Appl. **3**, e165 (2014).

31. N. Ji, "Adaptive optical fluorescence microscopy," Nat. Methods **14**, 374 (2017).

32. K. M. Hampson, R. Turcotte, D. T. Miller, *et al.*, "Adaptive optics for high-resolution imaging," Nat. Rev. Methods Primers **1**, 68 (2021).

33. Q. Zhang, Q. Hu, C. Berlage, *et al.*, "Adaptive optics for optical microscopy [invited]," Biomed. Opt. Express **14**, 1732–1756 (2023).

34. O. Albert, L. Sherman, G. Mourou, *et al.*, "Smart microscope: an adaptive optics learning system for aberration correction in multiphoton confocal microscopy," Opt. Lett. **25**, 52–54 (2000).

35. L. Sherman, J. Ye, O. Albert, *et al.*, "Adaptive correction of depth-induced aberrations in multiphoton scanning microscopy using a deformable mirror," J. Microsc. **206**, 65–71 (2002).

36. P. Marsh, D. Burns, and J. Girkin, "Practical implementation of adaptive optics in multiphoton microscopy," Opt. Express **11**, 1123–1130 (2003).

37. A. J. Wright, D. Burns, B. A. Patterson, *et al.*, "Exploration of the optimisation algorithms used in the implementation of adaptive optics in confocal and multiphoton microscopy," Microsc. Res. Tech. **67**, 36–44 (2005).

38. M. Skorsetz, P. Artal, and J. M. Bueno, "Performance evaluation of a sensorless adaptive optics multiphoton microscope," J. Microsc. **261**, 249–258 (2016).

39. P. Galwaduge, S. Kim, L. Grosberg, *et al.*, "Simple wavefront correction framework for two-photon microscopy of in-vivo brain," Biomed. Opt. Express **6**, 2997–3013 (2015).

40. M. Žurauskas, I. M. Dobbie, R. M. Parton, *et al.*, "IsoSense: frequency enhanced sensorless adaptive optics through structured illumination," Optica **6**, 370–379 (2019).

41. D. Débarre, M. J. Booth, and T. Wilson, "Image based adaptive optics through optimisation of low spatial frequencies," Opt. Express **15**, 8176–8190 (2007).

42. D. Débarre, E. J. Botcherby, T. Watanabe, *et al.*, "Image-based adaptive optics for two-photon microscopy," Opt. Lett. **34**, 2495–2497 (2009).

43. M. Jiang, X. Zhang, C. A. Puliafito, *et al.*, "Adaptive optics photoacoustic microscopy," Opt. Express **18**, 21770–21776 (2010).

44. Y. Notsuka, M. Kurihara, N. Hashimoto, *et al.*, "Improvement of spatial resolution in photoacoustic microscopy using transmissive adaptive optics with a low-frequency ultrasound transducer," Opt. Express **30**, 2933–2948 (2022).

45. K. Hampson, J. Antonello, R. Lane, *et al.*, "Sensorless Adaptive Optics (1.3)," Zenodo https://doi.org/10.5281/zenodo.4271425 (2020).

46. V. N. Mahajan and G.-M. Dai, "Orthonormal polynomials in wavefront analysis: analytical solution," J. Opt. Soc. Am. A **24**, 2994–3016 (2007).

47. M. Azimipour, F. Atry, and R. Pashaie, "Calibration of digital optical phase conjugation setups based on orthonormal rectangular polynomials," Appl. Opt. **55**, 2873–2880 (2016).

48. A. Hemphill, Y. Shen, J. Hwang, *et al.*, "High-speed alignment optimization of digital optical phase conjugation systems based on autocovariance analysis in conjunction with orthonormal rectangular polynomials," J. Biomed. Opt. **24**, 031004 (2018).

49. I. M. Vellekoop and A. P. Mosk, "Focusing coherent light through opaque strongly scattering media," Opt. Lett. **32**, 2309–2311 (2007).

50. D. B. Conkey, A. M. Caravaca-Aguirre, J. D. Dove, *et al.*, "Super-resolution photoacoustic imaging through a scattering wall," Nat. Commun. **6**, 7902 (2015).

51. P. Lai, L. Wang, J. W. Tay, *et al.*, "Photoacoustically guided wavefront shaping for enhanced optical focusing in scattering media," Nat. Photonics **9**, 126–132 (2015).

52. Z. Yu, H. Li, T. Zhong, *et al.*,"Wavefront shaping: A versatile tool to conquer multiple scattering in multidisciplinary fields," The Innovation **3**, 100292 (2022).

53. L. V. Wang, *Photoacoustic Imaging and Spectroscopy* (CRC Press, 2017).

54. Y. Liang, H. Liu, Q. Li, *et al.*, "Acoustic-spectrum-compensated photoacoustic microscopy," Opt. Lett. **45**, 1850–1853 (2020).

55. S. Chandramoorthi, J. J. M. Riksen, A. V. Nikolaev, *et al.*, "Wideband photoacoustic imaging in vivo with complementary frequency conventional ultrasound transducers," Front. Phys. **10**, 954537 (2022).

56. O. Tzang, E. Niv, S. Singh, *et al.*, "Wavefront shaping in complex media at 350 KHz with a 1D-to-2D transform," Nat. Photonics **13**, 788–793 (2018).

57. B. Blochet, L. Bourdieu, and S. Gigan, "Focusing light through dynamical samples using fast continuous wavefront optimization," Opt. Lett. **42**, 4994–4997 (2017).

58. D. B. Conkey, A. M. Caravaca-Aguirre, and R. Piestun, "High-speed scattering medium characterization with application to focusing light through turbid media," Opt. Express **20**, 1733–1740 (2012).

59. D. Wang, E. H. Zhou, J. Brake, *et al.*, "Focusing through dynamic tissue with millisecond digital optical phase conjugation," Optica **2**, 728–735 (2015).

60. C. Yeh, B. T. Soetikno, S. Hu, *et al.*, "Microvascular quantification based on contour-scanning photoacoustic microscopy," J. Biomed. Opt. **19**, 096011 (2014).

61. K. Maslov, G. Stoica, and L. V. Wang, "In vivo dark-field reflection-mode photoacoustic microscopy," Opt. Lett. **30**, 625–627 (2005).

62. B. Ning, M. J. Kennedy, A. J. Dixon, *et al.*, "Simultaneous photoacoustic microscopy of microvascular anatomy, oxygen saturation, and blood flow," Opt. Lett. **40**, 910–913 (2015).

63. X. Zhu, Q. Huang, A. DiSpirito, *et al.*, "Real-time whole-brain imaging of hemodynamics and oxygenation at micro-vessel resolution with ultrafast wide-field photoacoustic microscopy," Light Sci. Appl. **11**, 138 (2022).